Nano Energy 31 (2017) 74–83

Contents lists available at ScienceDirect

Nano Energy

journal homepage: www.elsevier.com/locate/nanoen

Fe_3N constrained inside C nanocages as an anode for Li-ion batteries through post-synthesis nitridation

Hao Huang[a,*,1], Song Gao[a,1], Ai-Min Wu[a], Kai Cheng[b], Xiao-Na Li[a], Xiao-Xia Gao[a], Ji-Jun Zhao[b], Xing-Long Dong[a], Guo-Zhong Cao[a,c]

[a] Key Laboratory of Materials Modification by Laser, Ion and Electron Beams (Ministry of Education), School of Materials Science and Engineering, Dalian University of Technology, Dalian 116024, China

[b] Key Laboratory of Materials Modification by Laser, Ion and Electron Beams (Ministry of Education), Dalian University of Technology, Dalian 116024, China

[c] Department of Materials Science and Engineering, University of Washington, Seattle, WA 98195, USA

ARTICLE INFO

Keywords:
Transition metal nitride
Core-shell nanoparticles
Electrochemical performance
Anode
Li-ion battery

ABSTRACT

Carbon-constraint Fe_3N nanoparticles (Fe_3N@C) with a unique core-shell structure are successfully realized through a facile 2-step process: fabricating Fe@C core-shell nanoparticles by DC arc-discharge method and subsequently converting them into Fe_3N@C through chemical nitriding reactions. A series of technological conditions are carried out to manipulate the core components and the shell structure. Owing to the protection of carbon shell, the nanoparticles own clear morphology and fine dispersion without distinct sintering. The Fe_3N@C nanoparticles are applied as the anode material for lithium-ion batteries and exhibit high electric capacity in long-term cyclic charge/discharge process. Their excellent performance comes from the electrochemical lithiation/delithiation reactivity of the Fe_3N core, while stable nanostructure of the electrodes sustained in the long cycles benefits from the constraint of carbon shell mostly.

1. Introduction

Rechargeable lithium-ion batteries (RLIBs) have been considered as one of the most promising energy storage system for a wide variety of applications including portable electronic devices and electric vehicles due to their high gravimetric and volumetric energy, high power density, long cycle life and low self-discharge properties [1], though other energy storage technologies are in a rapid development such as sodium and magnesium ion batteries [2], lithium-sulfur batteries [3] and metal-oxygen batteries [4]. The practical energy density of current commercial RLIBs, where graphite is currently utilized as the anode material [5], cannot keep up with the growing demand from high-power unplugged electronics. To cater to such requirements, exploration of new electrode materials is crucial for newly developed RLIBs with high capacity and excellent stability. Substantial efforts have been made in the attempts at various electrode materials, including alloy nanoparticles [6–8], carbon materials and transition metal compounds [9–14], most of which own attractive specific capacity and acceptable cyclic stability.

Among these materials, transition metal nitrides have aroused increasing interest due to their outstanding electrochemical properties, high chemical stability, standard technological approach and extensive fundamental importance [15–21]. Specific electronic configuration of the transition element (Group IIIB-VIII) is characterized by the fact that the valance electrons can occupy the partially-filled *d* orbitals due to their less-different energy levels between 4s and 3d, 5s and 4d or 6s and 5d. When the nitrides participate the redox reactions, multi-valence states are created to store energy effectively, as it has been reported in many previous studies focused on bi- or multi-nitrides [22–29] and nitride-based composites [30–32]. Nevertheless, up to now, the nitrides working as active material are still far from their practical application due to their large volume change resulting in fast capacity decay during the cyclic electrochemical reactions.

Two strategies, *i.e.* reducing the size of electrode active materials into nanoscale or forming a composite with carbon, have been widely studied to accommodate large varied volume and improve cyclic ability of the electrodes [33]. Several positive features can be expected and have been formerly approved in literatures. 1) Small size of the active material can shorten the diffusion route and storage time (t_s, t_s varies according to $\propto L^2$, where L is the length of ion diffusion.) of Li ions in the electrode materials and effectively reduce the mechanical stress [34]; 2) Various carbon frames, including graphite, carbon nanotubes,

* Corresponding author.
E-mail address: huanghao@dlut.edu.cn (H. Huang).
[1] These authors contributed equally.

http://dx.doi.org/10.1016/j.nanoen.2016.10.059
Received 15 July 2016; Received in revised form 12 October 2016; Accepted 27 October 2016
Available online 05 November 2016

3D carbon foam and *etc.*, have been applied to build elaborate nanocomposite with active materials, such as Fe-Sn(C) [6], C/CNTs/NiO [35], FeN/N-RGO [12], MoS_2/Graphene foam [36] and *etc.* The carbon exhibits practical function of buffering the excessive volume change of the active materials during the cyclic lithiation/delithiation process; 3) The carbon materials independently contribute to part of the battery capacity due to their own Li-ion storage ability. At the same time, they improve the conductivity of electrode and can help deliver the electrons generated during the redox reaction of the active materials to the electric collector. For example, Y. X. Tong *et al.* [32] adopted a simple two-step strategy to fabricate 3D flexible Ni_3N/carbon composites cloth successfully, which demonstrated fast electron transport and facile ion diffusion paths during the electrochemical reactions. The strategies on all accounts can be well-utilized for acquiring an optimal-designed nanostructure which can be charged/discharged steadily in high volume and at high rates.

In present work, a simple two-step synthetic route is proposed to fabricate the carbon-constraint Fe_3N nanostructure. The core-shell type of Fe@C nanoparticles, primarily as the precursor for the succeeding nitriding process, is manufactured in the DC arc-discharge plasma - a physical technique which has been adopted to produce metallic nanoparticles in high purity and in large yield (over kilogram per day under continuous operation). The Fe@C precursors are served as the starting material heat-treated in NH_3 environment at various temperatures. The Fe core of the Fe@C nanoparticle reacts into Fe_3N inside of the carbon cages which separate the metallic cores away from being sintered during the nitriding process. A unique nanostructure of carbon-constraint Fe_3N (Fe_3N@C) is finally acquired in such an easy and feasible way that could hardly be achieved by wet chemistry. When set as the anode material for RLIBs, the synthesized Fe_3N@C nanoparticles display excellent electrochemical properties with impressive initial Coulombic efficiency and outstanding stability. The superior cyclic performance and high reversible capacity are attributed to the carbon coatings, the rigid structure and strong mechanical strength of which play a significant role in buffering the volume variation and stabilizing the electrode reactions as well.

2. Experimental section

2.1. Synthesis of Fe_3N@C nanoparticles

The Fe@C nanoparticles were produced by DC arc-discharge method with a Fe bulk as anode, while a tungsten rod served as cathode of the device. The structure diagram of the arc-discharge equipment is shown in Fig. S1. The mixed atmosphere, methane and argon in a volume ratio of 1:2, was introduced into the pre-vacuumed chamber as the working gas. After the arc was ignited, the Fe bulk was evaporated into nanoparticles at a steady current of 90 A and the voltage was maintained at about 30 V by the electrical power supply. The space between two electrodes was continuously monitored in order to prevent the arc interruption due to the consumption of Fe bulk in the evaporation process. After a serial process of condensation, stabilization and passivation, the Fe@C nanoparticles were collected from the water-cooled chamber wall and confirmed in our former research as a core-shell structure with the Fe cores constrained in the onion-like carbon cages [37]. We weighed a proper amount (0.1 g) of the Fe@C powders and loaded them into Elemental Analyze (Germany Elementar Vario El III). After it was combusted in O_2 atmosphere, the carbon content in the sample was evaluated according to the CO_2 releasing amount and confirmed as about 29.2 wt% in this work.

The successive nitridation was conducted in a horizontal tube furnace and the protocol for the reactions was set as follows. Firstly, a proper amount (0.25 g) of the Fe@C nanoparticles powers were laid in an alumina crucible and carefully placed in the middle of the quartz tube. The system was evacuated (−0.1 MPa), then heated up to 100 °C for 30 min to remove the moisture adhering to the particles surface. Subsequently, NH_3 was introduced through molecular sieve into the vacuumed tube with a gas pressure of 0.06 MPa. After being stabilized for 15 min, the nanoparticles were heated up to 200 °C and maintained for 1 h. The other samples were prepared following the above procedure and then heated up to various temperatures preset at 300 °C (1 h), 400 °C (1 h) for and 500 °C (1 h and 2 h), respectively. Afterwards, the system was re-vacuumed and naturally cooled to the room temperature. The final products were then collected for various inspections.

2.2. Characterization

The crystal structure of the samples was characterized by X-ray diffraction (XRD-6000) using Cu Ka radiation (λ=1.5416 Å) at the scale of 20°–80°. The morphology and microstructure of the samples were analyzed using Transmission Electron Microscopy (TEM, Tecnai220 S-TWIM). X-ray Photoelectron Spectroscopy (XPS, Thermo Escalab 250Xi) utilizing monochromatic Al Kα ($h\upsilon$=1486.6 eV) radiation as theta probe was adopted to analyze the surface species on Fe@C and Fe_3N@C (400 °C 1 h) nanoparticles.

2.3. Electrochemical property measurements

Electrochemical performance was characterized on CR2025-type half-coin cells. The working electrodes were prepared by mixing the active material of the nanoparticles (80 wt%), conducting agent (Super P; Power Source Battery Co., Taiyuan) (10 wt%) and polyvinylidene fluoride (10 wt%) dissolved in N-methyl pyrrolidinone as a binder. All components were mixed together evenly to form slurry and then coated onto the copper foil substrates with the active materials (Fe_3N@C nanoparticles) mass loading about 0.6–1.2 mg cm^{-2}. These substrates were dried at 120 °C for 24 h in a vacuum oven and then cut into several circular pieces with a diameter of 14 mm as the test electrodes. The half-cells were assembled in an argon-filled glove box with the contents of moisture and oxygen both less than 0.1 ppm. The metallic lithium sheet was used as the counter electrode, 1 M $LiPF_6$ in ethylene carbonate/diethyl carbonate (1:1, v/v) as the electrolyte, and a polypropylene film as the separator. Cycling performance was performed on Land CT2001A test system. Cyclic voltammogram (CV) and electrochemical impedance spectroscopy (EIS) of the electrodes were measured by CHI 660D workstation. The charge/discharge behaviors were performed galvanostatically with a voltage window of 0.01–2.00 V (*vs.* Li/Li^+) at a current of 100 mA g^{-1}. CV measurements of the electrodes were conducted with a scan rate of 0.1 mV s^{-1} between 0.01–2.00 V. EIS was carried out at a 5 mV amplitude signal in the frequency range of 0.01 Hz-100 kHz.

3. Results and discussion

3.1. Crystal structure and morphology of Fe_3N@C nanoparticles

In order to ascertain the structure evolution of Fe@C nanoparticles during the nitriding process, the X-ray diffraction (XRD) inspections are performed and the patterns are shown in Fig. 1(a1-a5). Different reaction temperature and time are selected to the identical starting material. By comparing to the XRD spectra of Fe@C nanoparticles, it is clearly seen that the Fe cores begin their nitridation at a temperature as low as 200 °C. In Fig. 1(a1), the characteristic diffraction peaks located at 43.5°, 50.6° and 74.6° are related to the (111), (200) and (220) planes of $FeN_{0.0324}$ (JCPDS 75-2127), respectively. The $FeN_{0.0324}$ has

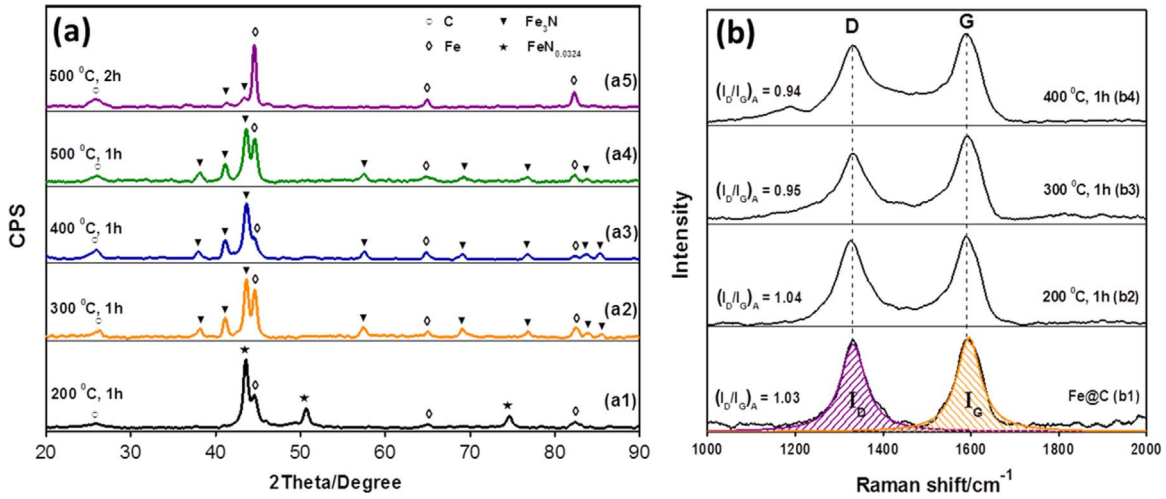

Fig. 1. XRD patterns of nitrided starting material Fe@C nanoparticles at 200 °C (a1), 300 °C (a2), 400 °C (a3), 500 °C (a4) for 1 h and 500 °C (a5) for 2 h, respectively. Raman spectra of starting material Fe@C nanoparticles (b1) and the nitrided Fe@C nanoparticles at 200 °C (b2), 300 °C (b3) and 400 °C (b4) for 1 h, respectively.

FCC structure with the cell parameters of *a=b=c=3.594 Å* and Fe has a known BCC structure of *a=b=c=2.860 Å*. It is suggested that the cores of the particles maintain their cubic structure with enlarged lattice constants till the nitriding temperature of 200 °C. Contrasting to the Fe@C XRD pattern, the Fe core is partially nitrided into ε-Fe_3N (JCPDS 001-1236) at 300 °C (Fig. 1(a2)). The nitridation keeps going on up to the temperature of 400 °C (Fig. 1(a3)), as it is indicated from the weakened peak of pure Fe. The identified characteristic peaks at 37.9°, 41.1° and 43.7° strongly illustrate that Fe_3N becomes the dominant phase occupying about 57% weigh ratio of the sample (a semi-quantitative analysis can be found in Fig. S2). If the temperature increases further to 500 °C and retains respectively for 1 h and 2 h, it is found that the peak intensity of pure Fe (44.6°) has enhanced in Fig. 1(a4, a5), due to the decomposition of Fe_3N. In this period, the reverse reaction of Fe_3N pyrolyzed into Fe is more efficient than the nitriding reaction. The Fe_3N is almost full-decomposed after 2 h and the cores transform back to Fe domains (Fig. 1(a5)).

According to the original work by K. H. Jack [38], $FeN_{0.0324}$ was obtained by gas nitriding 300-mesh Fe powder at 700 °C. Our experiments show that the nitridation of Fe nanoparticles initiates at a low temperature of 200 °C, which is an unsure reaction from the thermodynamic view, because the Gibbs-free-energy change of the reactions is positive at the temperature of 200 °C [39]. In this case, two reasons may make the low-temperature nitridation possible. The first is the intensive catalytic effect from the less-oxidized Fe surface protected by the carbon shell, so that NH_3 molecules can be easily dissociated into [N] and [H] atoms [40]. The chemisorption and formation of Fe-N bonds are enhanced on the nano-size Fe surface. The second contribution comes from the large excess stored energy in nano-crystalline grain boundaries or in-grain defects. Our starting material, Fe@C nanoparticles, was prepared in the arc-discharge plasma and experienced large temperature variation during its formation. Hence, large amount of defects and dislocations are left in the grain or at the grain boundaries, which provides an extra driving force for the nitriding reactions and even facilitates the diffusion of [N] atoms from particle surface to particle interior. The schematic diagram of the nitriding process is illustrated in Fig. S3. The structure of the carbon shell is analyzed by Raman spectra, as shown in Fig. 1(b). Two intensive peaks are allocated at about 1327.6 cm^{-1} and 1591.8 cm^{-1}, corresponding to the D peak (A_{1g} carbon vibration modes) and G peak (E_{2g} carbon vibration modes) respectively. Strong D-peak, normally aroused by the presence of in-plane substitutional heteroatoms, vacancies, grain boundaries or other defects, indicates a large amount of disordered carbon existing in the carbon shell, as it is observed in Fig. 1(b1-b4). The G-band is typical for graphite and carbon blacks, originated from the stretching vibration of any C pairs of sp^2 sites. Moreover, the graphite grain size in the expression of the in-plane correlation length, L_a, can be determined by the Tuinstra-Koenig equation [41].

$$L_a = C_\lambda (I_D/I_G)_A^{-1} \quad (1)$$

where C_λ is about 4.4 nm. $(I_D/I_G)_A$ can be obtained from the area ratio of D and G peaks after a Lorentzian function fitting with the Raman curve, the values of which are listed as 1.03, 1.04, 0.95, 0.94 respectively for the Fe@C precursor and the nitride products. After being calculated in Eq. (1), the values of L_a are given as 4.27 nm (Fe@C), 4.23 nm (200 °C), 5.12 nm (300 °C) and 5.24 nm (400 °C). The structure of carbon shell coated on nanoparticles is almost invariant under 200 °C heating. With the temperature promoted beyond 300 °C, the crystallization of carbon shell is gradually improved by the expanding of graphite grain size accompanied with the elimination of finite carbon semicrystals or plane defects in the carbon shell.

The TEM and high-resolution TEM images showing the morphologies of the nitride products obtained at 200 °C (a), 300 °C (b), 400 °C (c) and 500 °C (d), are presented in Fig. 2. The FE-SEM morphology of the nanoparticles is also given in Fig. S4 for an overall configuration. The nanoparticles, owing to the protection of carbon shell, maintain the integrated core-shell structures well till high temperatures. In the close observation of a particle (Fig. 2(a)), the shells of nanoparticles are composed of onion-like carbon in uniform thickness of about 2 nm ($d_G^{(002)}$=0.341nm). The lattice spacing of the cores, after the inverse fast Fourier transformation, is measured as 0.181 nm, close assigning to the (200) plane of $FeN_{0.0324}$. With the temperature rising to 300 and 400 °C respectively, the carbon layers coated nanoparticles thicken to 3–5 nm, meanwhile, bulges can be found in local range of the carbon shell circled in dotted line. The lattice spacing of the cores is measured as around 0.236 nm corresponding to the (110) plane of Fe_3N. The precursor, Fe@C nanoparticles are produced by the arc-discharge plasma which evaporates the Fe bulk target into atom gas in a carbonaceous atmosphere. The [Fe] and [C] atoms then condense together as nanoparticles when they escape out of the central arc district. Carbon is actually supersaturated in the Fe lattice because the nanoparticles experience fast quenching during their movement from

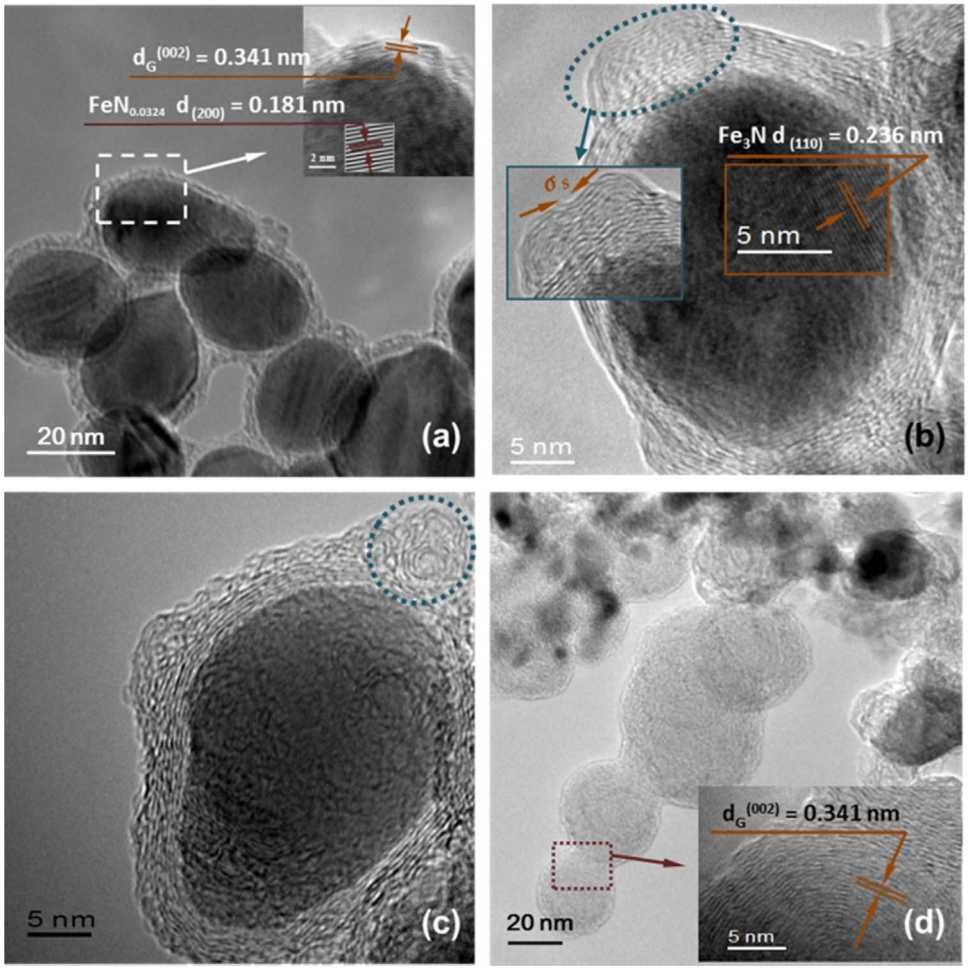

Fig. 2. TEM observation of the nitrided Fe@C nanoparticles by following reaction conditions: (a) 200 °C for 1 h; (b) 300 °C for 1 h; (c) 400 °C for 1 h; (d) 500 °C for 1 h.

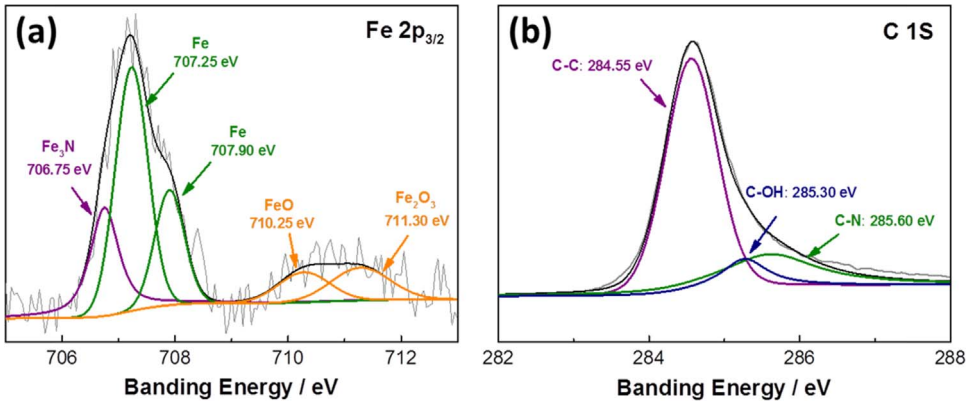

Fig. 3. High-resolution XPS of (a) Fe $2p_{3/2}$ and (b) C 1 s in Fe_3N@C (400 °C 1 h) nanoparticles.

the arc plasma to the water-cooled chamber wall. In the next step, the Fe cores of the nanoparticles are mildly nitrided into Fe_3N. The carbon atoms saturated in the Fe lattice are repelled outward into the carbon shell where considerable stress will be produced in-plane with the carbon layers. The normal stress concentrates at the largest convex curvature of the ellipsoid-like nanoparticles and creates serious deformation of the carbon layers, as it is illustrated in the inset of Fig. 2(b). With the process going on further, the bulges curl up in Fig. 2(c) to reduce the surfaces energy of the nanoparticles. When the temperature rises to 500 °C, curled carbon layers would gradually separate away from the surface of particles. Hence large amount of independent carbon nanoballs can be observed in the sample (Fig. 2(d)).

In order to identify the chemical composition, the XPS studies are carried out on the Ar-ion cleaned surface of the Fe_3N@C nanoparticles (400 °C 1 h) specimen. Fig. 3(a) and (b) illustrate the spectra for Fe and C elements respectively. The peaks at 284.55 and 285.30 eV for C 1s in Fig. 3(b) correspond to C–C bond and C–OH bond respectively. The C–C bond is related to the formation of π bond originated from sp^2

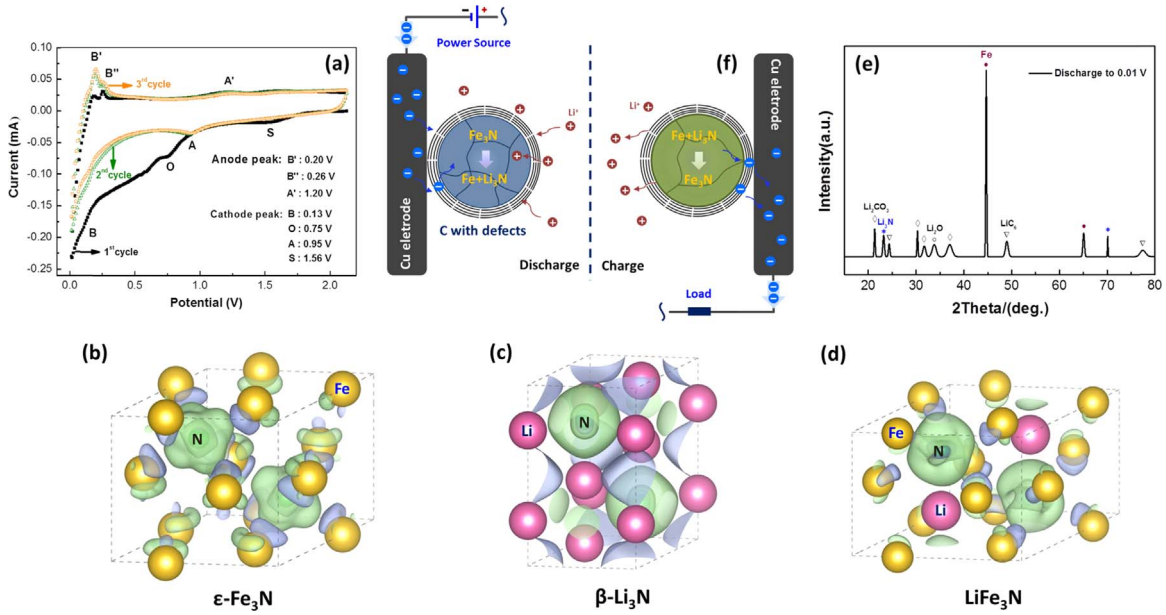

Fig. 4. (a) Cyclic voltammogram curves of Fe_3N@C (400 °C) nanoparticles electrode scanned between 0.01 and 2.00 V at a rate of 0.1 mV s^{-1}. Plots of electron density difference of (b) ε-Fe_3N, (c) β-Li_3N and (d) $LiFe_3N$. Isosurface value for electron density difference plots are 0.006 e/$Å^3$, where the accumulation and depletion of electron are represented in green and purple, respectively. The light yellow balls represent for [Fe] atoms, the light green balls for [N] atoms and the light pink balls for [Li] atoms. (e) XRD pattern of the Fe_3N@C (400 °C 1 h) electrode discharged to 0.01 V. (f) The mechanism figure of Fe_3N@C nanoparticles anode electrode during the charge/discharge process.

electronic configuration, while the sp^3 bond contained in the Raman spectrum is normally aroused by the presence of in-plane substitutional defects [42]. The C–OH bond has been discovered in the Fourier Transform Infrared spectroscopy of the carbon-coated nanoparticles or graphene made by DC arc-discharge method [43]. Fig. 3(a) is the binding energy related to Fe spectrum with different valance states. The peaks for Fe $2p_{3/2}$ located at 707.25 eV and 707.90 eV correspond to Fe. Peaks at around 706.75 eV, 710.25 eV and 711.30 eV are assigned to Fe_3N, FeO, and Fe_2O_3 respectively [44]. The oxides (FeO and Fe_2O_3), unable to be detected by XRD, is speculated to exist in small amount on the surface of Fe core, *i.e.* a spot between the Fe core and carbon shell. The remains of the oxides indicate that the NH_3 gas has not entirely reduce the oxide due to the handicap of the carbon shell. The reason can also be adopted to explain the inadequate nitridation of the Fe cores.

3.2. Electrochemical performance of the Fe_3N@C electrodes

Possessing the largest extent of active material Fe_3N, the sample nitrided at 400 °C is selected as the anode of Li-ion batteries. Fig. 4(a) shows the CV curves in the range of 0.01–2.00 V for the Fe_3N@C (400 °C 1 h) nanoparticles anode electrode. There are three reduction peaks (1.56 V (S), 0.75 V (O) and 0.13 V (B)) and three oxidation peaks (0.20 V (B′), 0.26 V (B") and 1.20 V (A′)) included in the initial curve respectively. The reduction peak at 1.56 V in the first discharging, which disappears in the subsequent cycles, corresponds to the formation of the solid electrolyte interface (SEI) [45]. The peak at 0.75 V (O) also appears only in the first run. This irreversible response correlates the reduction reaction of between the Fe oxides and Li ions, described in Eq. (2) [46]. The reduction peak at 0.13 V (B) and oxidation peaks at 0.20 V (B′) and 0.26 V (B") are associated with the insertion/desertion reactions between C and Li ions, which is described in Eq. (3) [47]. The peak intensity obviously enhances within the initial three cycles as the result of gradual infiltration of electrolyte into the active materials. In the curves, the reduction peak at 0.95 V (A) and the oxidation peak at 1.20 V (A′) imply the redox reactions between Fe_3N and Li ions [45,48]. In order to show the capacity retention and structure stability of the Fe_3N@C (400 °C 1 h) electrode, Four CV curves have been collected after the electrode is charged/discharged galvanostatically for 50 cycles, which is provided in Fig. S5.

$$Fe_xO + 2Li^+ + 2e^- \rightarrow xFe + Li_2O \quad (2)$$

$$6C + yLi^+ + ye^- \leftrightarrow Li_yC_6 \quad (3)$$

$$Fe_3N + 3Li^+ + 3e^- \leftrightarrow 3Fe + Li_3N \quad : \quad E_c = -1.19\ \text{eV (VASP)} \quad (4)$$

$$Fe_3N + Li^+ + e^- \leftrightarrow LiFe_3N \quad : \quad E_c = 2.69\ \text{ev (VASP)} \quad (5)$$

The identical lithiation reaction of the transition metal nitrides complies with $M_xN + xLi^+ + xe \rightarrow xM + Li_xN$ in many reported works [9,12,17]. Nevertheless, according to the original work of Z. W. Fu *et al.* [49], the lithium transition metal nitrides LiM_3N (M=Co, Ni, Cu and Fe), due to their lowest potential energies, have been considered as stable products during the lithiation process. Hence, here is the argument, *i.e.* which type of lithiation process the ε-Fe_3N should follow, Eq. (4) or Eq. (5). First-principle calculation is carried out to clarify this issue. BCC solid lithium is used to represent Li^+ and e^-. The Vienna Ab initio Simulation Package (VASP) is used by spin-polarized density functional theory. Based on the computation of both lithiation reactions of ε-Fe_3N, the chemical reaction heat (E_c) of Eq. (4) is calculated as −1.19 eV per Li atom (exothermic), while for Eq. (5), 2.69 eV is needed to realize in the endothermic-type lithiation reaction (more details are included in Fig. S6). The interaction between [N] and metal (Fe or Li) atoms in $LiFe_3N$, Fe_3N and β-Li_3N are characterized by the electron density difference. Compared with the Fe_3N (Fig. 4(b)) and β-Li_3N (Fig. 4(c)), more electrons clearly accumulate around [N] atoms in the β-Li_3N than that of the ε-Fe_3N, which indicates that the Li-N bonds in β-Li_3N are stronger than the Fe-N bonds in ε-Fe_3N. In other words, the Li atoms can easily replace the Fe atoms during the

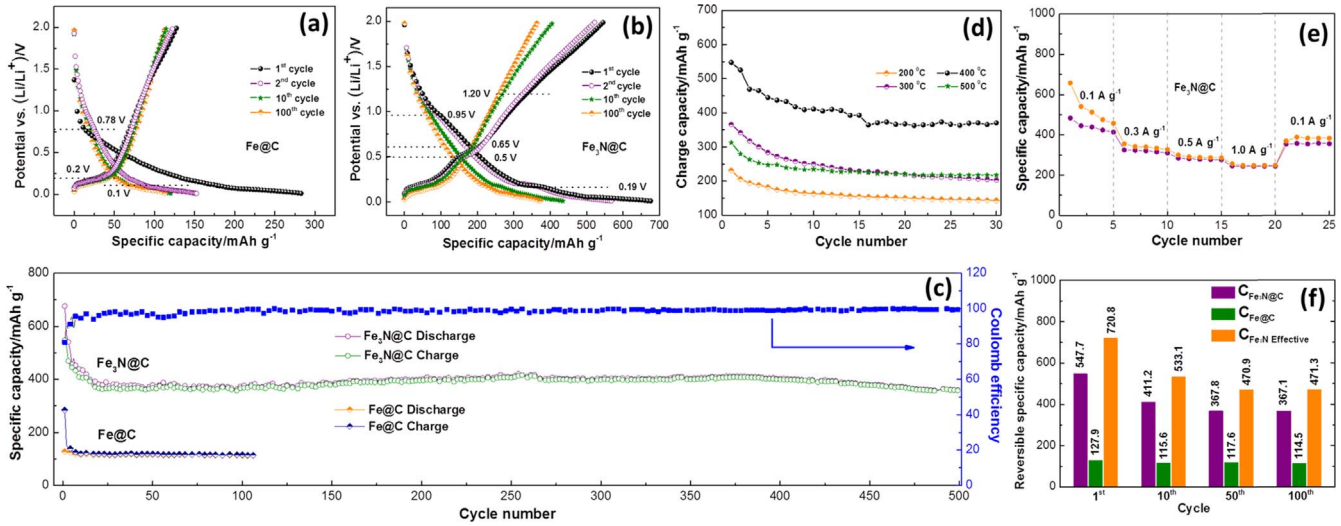

Fig. 5. Discharge/charge curves for (a) Fe@C and (b) Fe_3N@C nanoparticles, (c) cycling performance of Fe_3N@C and Fe@C nanoparticles anode electrodes. (d) Galvanostatic charge behaviors of the samples nitrided at 200 °C, 300 °C, 400 °C and 500 °C for 1 h, respectively. The measurement was carried out between 0.01 and 2.00 V at a rate of 100 mA g^{-1}. (e) Cycling performance of the Fe_3N@C nanoparticles (400 °C 1 h) electrode at different current densities from 0.1 to 1.0 A g^{-1} between 0.01–2.00 V. (f) Reversible capacity of in-core Fe_3N and carbon shell in electrode during the initial 100 cycles when Fe_3N@C (400 °C 1 h) is utilized.

lithiation process. However, for the $LiFe_3N$ (Fig. 4(d)), there is almost no exhaustion of electrons around Li atoms at the 0.006 e/Å^3 isosurface value level, as well as less charge transferring from [N] atoms to [Fe] atoms in the $LiFe_3N$ due to the lattice expansion during Li insertion process. According to the results of electron density difference, a conclusion can be drawn that the lithiation product, β-Li_3N, is more stable than the lithium transition metal nitride ($LiFe_3N$), *i.e.* the conversion reaction described in Eq. (4) can occur more easily from the energy point of view. In order to verify the lithiation products further, the XRD pattern of Fe_3N@C nanoparticles (400 °C 1 h) electrode which has been discharged to 0.01 V is studied and shown in Fig. 4(e). the peaks for Li_2CO_3, LiC_6 and Li_2O can be identified as the main components of the SEI [50,51]. Besides, the diffraction peaks located at 23.07° and 70.15° are related to the (001) and (112) planes of Li_3N (JCPDS 96-431-1894). Fe can find its strong peaks at the 44.61° and 65.08°. The products of the Fe_3N lithiation reaction can be clearly confirmed as Li_3N and Fe, which is well coincident with the first-principle calculation.

Fig. 4(f) illustrates the Li-ion insertion/desertion mechanism of the Fe_3N@C nanoparticles in which two active materials Fe_3N and C both participate the lithiation/delithiation. During the cathodic process, Fe_3N and C reacts with Li^+ at different potentials. The electrons required for the forward reactions in Eqs. (3–4) are provided by an electric source. The anodic process (delithiation) presents a reverse of the cathodic process. The Li ions return back into the electrolyte along with the generated electrons flowing to the load. Within the whole process, the carbon shell is of utmost importance to maintain the electrode working in high efficiency. (i) Large proportion of defects in the carbon shell, as observed in the TEM and Raman results, will allow the Li ions to infiltrate easily through and access the Fe_3N core for the lithiation reactions; (ii) Considering its conductivity, the carbon shell become the only path of electron transportation for the electrochemical reactions of Fe_3N; (iii) The constraint of carbon shell accommodate the excessive volume change of the Fe_3N cores during their cyclic lithiation/delithiation, and further protect the inside cores from pulverization and losing ohmic contacts.

In order to investigate the cycling performance of the Fe_3N@C nanoparticles anode, typical sloping voltage profiles are obtained in the potential range of 0.01–2.00 V and at a constant current density of 100 mA g^{-1}, as shown in Fig. 5(b). The identical test parameters are carried out to the counterpart of Fe@C nanoparticles, the specific capacity of which was obtained based on the weight of carbon measured by Elemental Analyzer (Germany Elementar Vario El III). The profiles of potential *vs.* specific capacity are presented in Fig. 5(a). In the 1st discharge curve of Fe_3N@C, the dynamic voltage plane from 1.6 to 1 V is assigned to the formation of SEI film [45]. The plane voltage at about 0.19 V is related to delithiation reaction between C and Li [47], which also can be found in the initial change profile of the Fe@C nanoparticles (Fig. 5(a)). In the charge curve of Fe_3N@C, the extra charge plane voltage region at about 0.5–0.65 V, compared with that of Fe@C, attributes to the formation of Fe_3N by the reaction between Fe and Li_3N [45]. Slight potential slopes can be also found at about 0.95 V and 1.20 V in subsequent discharge/charge curves under a close observation of Fig. 5(b), corresponding to the weak redox reaction between Fe_3N and Li ions in Fig. 4(a).

The initial discharge/charge capacity of the Fe_3N@C nanoparticles electrode is 676.2/547.7 mAh g^{-1} (Coulombic efficiency is about 80.9%). The capacity maintains at the level of about 370 mAh g^{-1} and exhibits satisfactory cyclic stability during 500 cycles (Fig. 5(c)). The electrochemical properties of other samples nitrided at 200 °C, 300 °C and 500 °C for 1 h, are examined in the galvanostatic test (voltage range of 0.01–2.00 V at a current density of 100 mA g^{-1}, same as the test condition of the 400 °C sample). As shown in the Fig. 5(d), the charge capacity of the samples increases when the nitriding temperature promotes from 200 to 400 °C (200 °C: 143 mAh g^{-1}, 300 °C: 203 mAh g^{-1} and 400 °C: 370 mAh g^{-1} at the 30th cycle), and it reaches the maximum value in the sample of Fe_3N@C (400 °C 1 h) where the Fe_3N phase, as the dominant capacity contributor, gains the largest occupation. With the nitriding temperature further increased to 500 °C, Fe_3N begins to decompose back into Fe, which also brings about expectant drop of the charge capacity (216 mAh g^{-1} at the 30th cycle). Further, the charge/discharge behaviors at different current densities are also studied for the Fe_3N@C nanoparticles and are shown in Fig. 5(e). With the current density increased from 0.1 to 1.0 A g^{-1}, average reversible capacity of the Fe_3N@C (400 °C 1 h) electrode exhibits a descending tendency from 450 to 244 mAh g^{-1}. When the

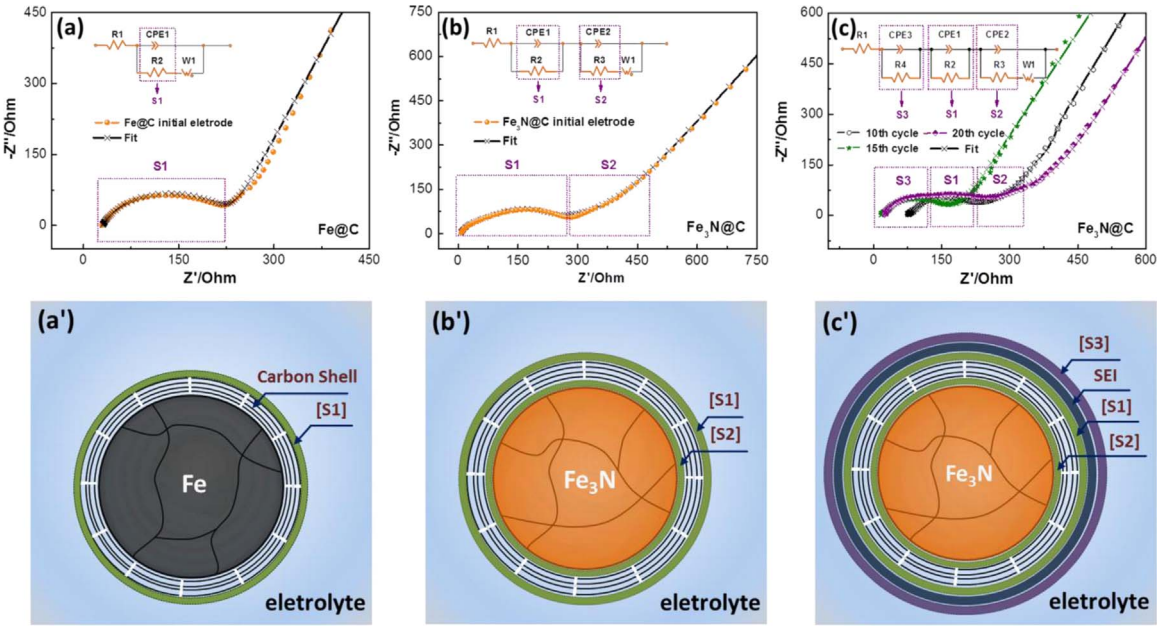

Fig. 6. The initial Nyquist plots of Fe@C nanoparticles (a) and the 1st (b), 10th and 20th (c) Nyquist plots of Fe_3N@C (400 °C 1 h) nanoparticles, as well as their equivalent circuit fitting and the corresponding models. (a′-c′) The corresponding simplified models of Fe@C nanoparticles and Fe_3N@C (400 °C 1 h) nanoparticles in various cycles. R_1, the electrolyte contact resistance (including the bulk resistance in the electrolyte, separator, and electrode). R_2, the lithium ions transfer resistance in the carbon shell of Fe@C or Fe_3N@C nanoparticles/electrolyte interface (S_1 [*CPE1*, R_2]). R_3, the charge transfer resistance in the interface of Fe_3N in Fe_3N@C nanoparticles/electrolyte (S_2 [*CPE2*, R_3]). R_4, the charge transfer resistance in the SEI film interface (S_3 [*CPE3*, R_4]). W_1, the Warburg charge diffusion processes of lithium ions in the Fe@C or Fe_3N@C nanoparticles electrodes. *CPE1*, the space charge capacitance in the carbon shell of Fe@C or Fe_3N@C nanoparticles/electrolyte interface. *CPE2*, the space charge capacitance in the Fe_3N in Fe_3N@C nanoparticles/electrolyte interface. *CPE3*, the space charge capacitance in the SEI film interface.

Table 1
Equivalent circuit parameters of Fe@C and Fe_3N@C nanoparticles electrodes.

Sample	*CPE1* (F)	*CPE2* (F)	*CPE3* (F)	R_2 (Ω)	R_3 (Ω)	R_4 (Ω)	σ_W (Ω cm^2 s$^{-0.5}$)	D_O (cm^2 s^{-1})	i_o (mA cm^{-2})
Fe@C Initial	3.05×10^{-5}	–	–	185.10	–	–	26.64	1.96×10^{-13}	8.92×10^{-2}
Fe_3N@C Initial	9.41×10^{-6}	4.61×10^{-6}	–	104.50	86.70	–	28.28	1.74×10^{-13}	1.60×10^{-1}
10th cycle	7.96×10^{-6}	4.20×10^{-3}	8.18×10^{-4}	57.88	58.90	181.30	23.55	2.51×10^{-13}	2.88×10^{-1}
15th cycle	6.59×10^{-6}	1.28×10^{-4}	1.84×10^{-4}	25.73	15.13	146.20	22.96	2.64×10^{-13}	6.49×10^{-1}
20th cycle	5.34×10^{-6}	5.24×10^{-6}	1.72×10^{-6}	19.80	12.36	143.90	19.77	3.56×10^{-13}	8.43×10^{-1}

current density returns to 0.1 A g^{-1}, the average capacity recoveries to about 354 mAh g^{-1}. The iron nitrides, as the anode material of Li-ion batteries, have been paid adequate attention to their electrochemical performance since the early century [45,52]. However, because of the drastic volume variation presented during the cyclic runs of charge/discharge, pure nitrides did not exhibit satisfactory capacity and extending life span. The performance of the Fe_3N nanoparticles is experimentally verified in Fig. S7. In order to improve the electrochemical performance of the iron nitrides, various strategies have been attempted in recent years. The most popular one is to composite with carbon materials, such as FeN/N-RGO [12], Fe_2N@C-RGO composite [19] and *etc*. They obtained greatly improved rate capability compared with the pure iron nitrides. However, the cyclic performance is still far from satisfaction due to the weak interference between the carbon and iron nitrides. In our case, strong constraint can be offered via a core-shell nanostructure. The carbon shell can effectively buffer the volume variation of the iron nitride core and stabilize the electrode reactions in long-term cycles. Likewise, the capacity in current work is not notable comparing to some recently reported anodes, such as Si-based ones [53,54]; nevertheless, it is still abundant to couple with a cathode whose capacity is still limited at the present. Anyway, for practical application, feasible synthetic route and long-term stability are the primary concerns for the selection of electrode materials.

For the purpose of figuring out the contribution of each active components, the specific capacity of Fe_3N@C ($C_{Fe_3N@C}$), carbon (C_C) and Fe_3N (C_{Fe_3N}) are plotted in the histogram of Fig. 5(f). C_C at different cycles is selected in the charge/discharge curves of Fe@C nanoparticles in Fig. 5(a). Assuming that the mass variation of C is neglected during the nitridation for an approximate analysis, the mass percent of C (δ_C) in the Fe_3N@C nanoparticles takes 29.2 wt% as that occupies in the Fe@C nanoparticles. Hence, C_{Fe_3N} can be calculated as $C_{Fe_3N}=\frac{C_{Fe_3N@C}-\delta_C\times C_C}{1-\delta_C}$. The capacities of the components are calculated at the 1st, 10th, 50th and 100th cycles respectively, the histogram of which is shown in Fig. 5(f). The capacity of C keeps invariant at about 115 mAh g^{-1}, while $C_{Fe_3N@C}$ witnesses a decrease along with C_{Fe_3N} before 50 cycles. C_{Fe_3N} is the dominant part and determines the variation of the total capacity of the Fe_3N nanoparticles. After 50 cycles, the values of C_{Fe_3N} keep less varied at about 470 mAh g^{-1} owing to the stabilized carbon-constraint nanostructure.

The interfacial properties of the Fe_3N@C (400 °C 1 h) nanoparticles electrode are measured by the EIS technic. The initial and subsequent

EIS (the 10th and 20th cycles), as well as corresponding equivalent circuit modeling and fitting plots are shown together in Fig. 6(b, c). It is found that the fitting plots agree well with the EIS of their electrodes each. The EIS of the Fe@C nanoparticles, illustrated in Fig. 6(a) for comparison, are composed of a depressed semicircle in the high frequency range (reflected at C/electrolyte interface, S_1) and a slope line at the low frequencies. For the initial EIS of Fe_3N@C nanoparticles, it consists of two depressed semicircles in the high and middle frequency ranges (reflected at S_1 and the interface of Fe_3N/electrolyte, S_2) (Fig. 6(b)). After 10 and 20 cycles of the Fe_3N@C nanoparticles electrode, the EIS are composed of three depressed semicircles in the high and middle frequency range, respectively, (reflected at S_1, S_2 and the interface of SEI film on surface of Fe_3N@C, S_3) and the Warburg impedance at the low frequencies (Fig. 6(c)).

In order to illustrate the correspondence between the EIS and the interfacial structure of the both particles, the Fe_3N@C and Fe@C nanoparticles are simplified into the regular concentric core-shell model, as shown in Fig. 6(a′-c′). The structure diagram of Fe@C nanoparticles (Fig. 6(a′)) is composed with carbon shell and Fe core. S_1 is assigned to the interface between the carbon shell and electrolyte, because the carbon shell is the only active material in Fe@C nanoparticles to react with Li ions during the initial cycle. As for the Fe_3N@C nanoparticles (Fig. 6(b′)), the carbon shell and Fe_3N core are both Li-active to participate in the reactions with Li ions. Hence, besides the C/electrolyte interface S_1, the interface S_2 can be defined at the Fe_3N/electrolyte which infiltrates through the breakage or defects of the carbon shell and forms interface around the Fe_3N core. After 10 and 20 cycles, the additional interface between SEI film and electrolyte (S_3) is included in the corresponding model as well (Fig. 6(c′)). The electrolyte contact resistance (R_1), charge transfer resistances (R_2-R_4), space charge capacitances (*CEP1*-*CEP3*) and Warburg impedance (W_1) are included in the fitting data of the EIS respectively. Faradic current density (I_F) of S_1 interface and the diffusion coefficient (D_O) of Li^+ are calculated in Eqs. (6–8) [55] and recorded in Table 1.

$$Z' = R_1 + R_{ct} + \sigma_w \omega^{-0.5} \tag{6}$$

$$I_F = \frac{RT}{nAFR_2} \tag{7}$$

$$D_0 = 0.5\left(\frac{RT}{AF^2\sigma_w C}\right)^2 \tag{8}$$

where R_{ct} is Li^+ transfer resistance, T is the room temperature (298 K), A is the contact area between the electrolyte and the electrode, F is the Faraday constant (9.6485×10^4 C mol^{-1}), σ_w is the Warburg coefficient, C is the molar concentration of Li^+ and n is the number of electrons transferred per molecule during the intercalation.

From the fitting results of the Fe@C nanoparticles and Fe_3N@C nanoparticles in Table 1, the R_2, *CEP1* and D_O values of the Fe@C nanoparticles at the initial cycle are larger than the Fe_3N@C nanoparticles and the I_F is smaller correspondingly, which ascribes to different infiltration degree of both systems in the initial cycle. After 20 cycles, the R_2 value, comparing with the first cycle of Fe_3N@C nanoparticles, reduces from 104.50 to 19.80 Ω, accompanied by its space charge capacitance *CEP1* decreased from 9.41×10^{-6} to 5.34×10^{-6} F; furthermore, the value of I_F increases from 1.60×10^{-1} to 8.43×10^{-1} mA cm^{-2}, which indicates that lower charge capacitance at the interface S_1, *i.e.* the breakdown of the formation of charge accumulation in the interface, could reduce the charge transfer resistance (R_2) [56,57]. During the first 20 cycles of the battery, R_4 drops from 181.3 to 143.9 Ω, and the space charge capacitance *CEP3* decreases from 8.18×10^{-4} to 1.724×10^{-6} F at interface S_3, because the SEI film, coated on the surface of particles, becomes gradually dense and complete during cycling process, which improves the conductive ability of interfacial carriers due to the pseudo-capacitance generated during the Li-ions insertion and extraction [58].

For the initial EIS of the Fe_3N@C, the small space charge capacitance (*CPE2*) of 1.724×10^{-6} F and high charge transfer resistance (R_2) of 86.7 Ω imply the weak ion transmission at the interface S_2. The value of *CPE2* at the 10th cycle raises to 4.2×10^{-3} F because the infiltration around the Fe_3N core is incomplete due to the resistant viscous flow of the electrolyte through the carbon shell. The *CPE2* and R_2 decrease sharply with the cycle proceeding when the free volume between the carbon shell and Fe_3N is fulfilled with the electrolyte and effective interface is setup to maintain equivalent Li-ion transfer. At 20th cycle where the electrode starts having a stable capacity (Fig. 5(c)), the *CPE2* (5.24×10^{-6} F) value at the interface S_2 is found exactly near to that of *CPE1* (5.34×10^{-6} F) at S_1, which infers that both S_1 and S_2 are the same type of C/electrolyte double-layer interfaces, but locate outside and inside of the carbon shell. The ion accumulation at S_2 interface, at the same time, creates local Li^+ concentration gradient that would fascinate the ion diffusion deeply into the Fe_3N cores and increase the driving force of the chemical diffusion of Li ions. In short, this kind of dual-capacitive interface, as it is defined for what has been described, plays an important role for the enhanced lithiation/delithiation ability in the Fe_3N@C.

4. Conclusion

Carbon-constraint Fe_3N@C nanostructure was successfully synthetized and controlled deliberately through manipulating a series of processing conditions, such as nitriding temperature and time. The sample nitrided at 400 °C was selected as the anode of Li-ion battery due to its largest extent of active material (Fe_3N). The as-prepared Fe_3N@C nanoparticles showed excellent electrochemical Li-ion storage properties with high initial charge/discharge capacity (545/675.8 mAh g^{-1} at a rate of 100 mA g^{-1}) and a superior cycle stability (a specific reversible capacity of 358 mAh g^{-1} maintained after 500 cycles). The energy storage features, according to the EIS analysis and first-principal calculation, were clarified including Fe_3N-dominant capacity, enhanced charge transportation and dual-capacitive interface of the carbon shell, the mechanism of which equally could be extended for the specific electrochemical behavior in carbon-constraint transition metal nitride nanostructures.

Acknowledgements

The authors gratefully acknowledge the support from the National Key Research and Development Program of China (Grant No. 2016YFB0101206), the National Natural Science Foundation of China (NSFC 51171033) and the Fundamental Research Funds for the Central Universities (DUT16LAB01, DUT16LAB03, DUT15LAB05).

Appendix A. Supporting information

Supplementary data associated with this article can be found in the online version at doi:10.1016/j.nanoen.2016.10.059.

References

[1] K. Kang, Y.S. Meng, J. Bréger, C.P. Grey, G. Ceder, Science 311 (2006) 977–980.
[2] R.C. Masse, E. Uchaker, G.Z. Cao, Sci. China Mater. 58 (2015) 715–766.
[3] G.M. Zhou, E. Paek, G.S. Hwang, A. Manthiram, Nat. Commun. 6 (7760) (2015)

1–11.
[4] J. Kim, H. Park, B. Lee, W.M. Seong, H.D. Lim, Y.J. Bae, H. Kim, W.K. Kim, K.H. Ryu, K. Kang, Nat. Commun. 7 (10670) (2015) 1–9.
[5] J.M. Tarascon, M. Armand, Nature 414 (2001) 359–367.
[6] C.J. Liu, F.H. Xue, H. Huang, X.H. Yu, C.J. Xie, M.S. Shi, G.Z. Cao, Y.G. Jung, X.L. Dong, Electrochim. Acta 129 (2014) 93–99.
[7] W.J. Zhang, J. Power Sources 196 (2011) 13–24.
[8] G. Wang, Z.W. Lu, X.P. Gao, X.J. Liu, J.Q. Wang, J. Power Sources 189 (2009) 655–659.
[9] S. Goriparti, E. Miele, F.D. Angelis, E.D. Fabrizio, R.P. Zaccaria, C. Capiglia, J. Power Sources 257 (2014) 421–443.
[10] L.W. Ji, Z. Lin, M. Alcoutlabi, X.W. Zhang, Energy Environ. Sci. 4 (2011) 2682–2699.
[11] G. Chen, R. Rodriguez, L. Fei, Y. Xu, S.G. Deng, S. Smirnov, H.M. Luo, J. Power Sources 259 (2014) 227–232.
[12] L.F. Lai, J.X. Zhu, B.S. Li, Y.D. Zhen, Z.X. Shen, Q.Y. Yan, J.Y. Lin, Electrochim. Acta 134 (2014) 28–34.
[13] N. Mahmood, C.Z. Zhang, Y.L. Hou, Small 9 (2013) 1321–1328.
[14] M. Zhang, T.H. Wang, G.Z. Cao, Int. Mater. Rev. 60 (2015) 330–352.
[15] S.M. Dong, X. Chen, X.Y. Zhang, G.L. Cui, Coord. Chem. Rev. 257 (2013) 1946–1956.
[16] D.K. Nandi, U.K. Sen, D. Choudhury, S. Mitra, S.K. Sarkar, ACS Appl. Mater. Interfaces 6 (2014) 6606–6615.
[17] M.S. Balogun, M.H. Yu, C. Li, T. Zhai, Y. Liu, X.H. Lu, Y.X. Tong, J. Mater. Chem. A 2 (2014) 10825–10829.
[18] M.S. Balogun, M.H. Yu, Y.C. Huang, C. Li, P.P. Fang, Y. Liu, X.H. Lu, Y.X. Tong, Nano Energy 11 (2015) 348–355.
[19] P. Yu, L. Wang, F.F. Sun, D.D. Zhao, C.G. Tian, L. Zhao, X. Liu, J.Q. Wang, H.G. Fu, Chem. Eur. J. 21 (2015) 3249–3256.
[20] M.S. Balogun, W.T. Qiu, W. Wang, P.P. Fang, X.H. Lu, Y.X. Tong, J. Mater. Chem. A 3 (2015) 1364–1387.
[21] Y. Zhong, X.H. Xia, F. Shi, J.Y. Zhan, J.P. Tu, H.J. Fan, Adv. Sci. 3 (1500286) (2016) 1–28.
[22] D. Kundu, F. Krumeich, R. Fotedar, R. Nesper, J. Power Sources 278 (2015) 608–613.
[23] D.K. Nandi, U.K. Sen, S. Sinha, A. Dhara, S. Mitra, S.K. Sarkar, Phys. Chem. Chem. Phys. 17 (2015) 17445–17453.
[24] R.C.D. Guzman, J.H. Yang, M.M.C. Cheng, S.O. Salley, K.Y.S. Ng, J. Mater. Chem. A 2 (2014) 14577–14584.
[25] T. Song, K.C. Kil, Y. Jeon, S. Lee, W.C. Shin, B. Chung, K. Kwon, U. Paik, J. Power Sources 253 (2014) 282–286.
[26] M.S. Balogun, W.T. Qiu, J.H. Jian, Y.C. Huang, Y. Luo, H. Yang, C.L. Liang, X.H. Lu, Y.X. Tong, ACS Appl. Mater. Interfaces 7 (2015) 23205–23215.
[27] C.W.B. Bezerra, L. Zhang, K.C. Lee, H.S. Liu, A.L.B. Marques, E.P. Marques, H.J. Wang, J.J. Zhang, Electrochim. Acta 53 (2008) 4937–4951.
[28] S.M. Dong, X. Chen, L. Gu, X.H. Zhou, H.X. Xu, H.B. Wang, Z.H. Liu, P.X. Han, J.H. Yao, L. Wang, G.L. Cui, L.Q. Chen, ACS Appl. Mater. Interfaces 3 (2011) 93–98.
[29] X.H. Lu, G.M. Wang, T. Zhai, M.H. Yu, S.L. Xie, Y.C. Ling, C.L. Liang, Y.X. Tong, Y. Li, Nano Lett. 12 (2012) 5376–5381.
[30] X.H. Zhou, C.Q. Shang, L. Gu, S.M. Dong, X. Chen, P.X. Han, L.F. Li, J.H. Yao, Z.H. Liu, H.X. Xu, Y.W. Zhu, G.L. Cui, ACS Appl. Mater. Interface 3 (2011) 3058–3063.
[31] M.S. Balogun, Z.P. Wu, Y. Luo, W.T. Qiu, X.L. Fan, B. Long, M. Huang, P. Liu, Y.X. Tong, J. Power Sources 308 (2016) 7–17.
[32] M.S. Balogun, Y.X. Zeng, W.T. Qiu, Y. Luo, A. Onasanya, T.K. Olaniyi, Y.X. Tong, J. Mater. Chem. A 4 (2016) 9844–9849.
[33] Q.F. Zhang, E. Uchaker, S.L. Candelaria, G.Z. Cao, Chem. Soc. Rev. 42 (2013) 3127–3171.
[34] J. Maier, J. Power Sources 174 (2007) 569–574.
[35] W.W. Liu, C.X. Lu, X.L. Wang, K. Liang, B.K. Tay, J. Mater. Chem. A 3 (2015) 624–633.
[36] J. Wang, J.L. Liu, D.L. Chao, J.X. Yan, J.Y. Lin, Z.X. Shen, Adv. Mater. 26 (2014) 7162–7169.
[37] X.F. Zhang, X.L. Dong, H. Huang, B. Lv, J.P. Lei, C.J. Choi, J. Phys. D: Appl. Phys. 40 (2007) 5383–5387.
[38] K.H. Jack, Proc. R. Lond. A 208 (1951) 200–214.
[39] W.P. Tong, N.R. Tao, Z.B. Wang, J. Lu, K. Lu, Science 299 (2003) 686–688.
[40] P. Schaaf, Prog. Mater. Sci. 47 (2002) 1–161.
[41] C.J. Liu, H. Huang, G.Z. Cao, F.H. Xue, R.A.P. Camacho, X.L. Dong, Electrochim. Acta 144 (2014) 376–382.
[42] X.W. Liu, Y. Wu, Z.Z. Yang, F.S. Pan, X.W. Zhong, J.Q. Wang, L. Gu, Y. Yu, J. Power Sources 293 (2015) 799–805.
[43] G.F. Guo, H. Huang, F.H. Xue, C.J. Liu, H.T. Yu, X. Quan, X.L. Dong, Surf. Coat. Technol. 228 (2013) 120–125.
[44] Y.B. Li, Y.R. Yan, H. Ming, J.W. Zheng, Appl. Surf. Sci. 305 (2014) 683–688.
[45] Z.W. Fu, Y. Wang, X.L. Yue, S.L. Zhao, Q.Z. Qin, J. Phys. Chem. B 108 (2004) 2236–2244.
[46] C.X. Wang, G.J. Shao, Z.P. Ma, S. Liu, W. Song, J.J. Song, Electrochim. Acta 130 (2014) 679–688.
[47] J.H. Lee, B.S. Kong, S.B. Yang, H.T. Jung, J. Power Sources 194 (2009) 520–525.
[48] T. Yoon, C.J. Chae, Y.K. Sun, X. Zhao, H.H. Kung, J.K. Lee, J. Mater. Chem. 21 (2011) 17325–17330.
[49] J. Ma, L. Yu, Z.W. Fu, Electrochim. Acta 51 (2006) 4802–4814.
[50] K. Leung, F. Soto, K. Hankins, P.B. Balbuena, K.L. Harrison, J. Phys. Chem. C 120 (2016) 6302–6313.
[51] L. Benitez, D. Cristancho, J.M. Seminario, J.M.M.D.L. Hoz, P.B. Balbuena, Electrochim. Acta 140 (2014) 250–257.
[52] J.L.C. Rowsell, V. Pralong, L.F. Nazar, J. Am. Chem. Soc. 123 (2001) 8598–8599.
[53] D.M. Piper, J.J. Travis, M. Young, S.B. Son, S.C. Kim, K.H. Oh, S.M. George, C.M. Ban, S.H. Lee, Adv. Mater. 26 (2014) 1596–1601.
[54] D.C. Lin, Z.D. Lu, P.C. Hsu, H.R. Lee, N. Liu, J. Zhao, H.T. Wang, C. Liu, Y. Cui, Energy Environ. Sci. 8 (2015) 2371–2376.
[55] Y. Cui, X.L. Zhao, R.S. Guo, Electrochim. Acta 55 (2010) 922–926.
[56] T. Xia, W. Zhang, J. Murowchick, G. Liu, X.B. Chen, Nano Lett. 13 (2013) 5289–5296.
[57] Y.M. Liu, H.T. Yu, X. Quan, S. Chen, H.M. Zhao, Y.B. Zhang, Sci. Rep. 4 (6843) (2014) 1–6.
[58] T. Li, Y.Y. Wang, R. Tang, Y.X. Qi, N. Lun, Y.J. Bai, R.H. Fan, ACS Appl. Mater. Interfaces 5 (2013) 9470–9477.

Hao Huang is a professor in school of Materials Science and Engineering, Dalian University of Technology (DUT). He obtained his Ph.D. degree at Changwon National University (South Korea) and was employed by DUT in 2005. He initiated Energy Materials & Devices Laboratory in 2015, majoring in high-performance electrode materials. Plasmatic physical methods (DC arc discharge, Microwave-plasma CVD, Magnetron sputtering, High-current pulsed electron beam and *etc.*) are utilized to design multi-type nanomaterials including nanoparticles, nanofilm and nanocomposite as the active materials for long-term and high-density energy storage in batteries (Li-ion, Li-S and Li-O_2), supercapacitors and fuel cells.

Song Gao was born in Liao Ning, China in 1987. He is currently a Ph.D. student under the supervision of Prof. H. Huang at Energy Materials & Devices Laboratory, School of Materials Science and Engineering in Dalian University of Technology. During 2012–2013, he studied as a co-culture student in Suzhou Institute of Nano-Tech and Nano-Bionics (SINANO), Chinese Academy of Sciences. His current research is focused on the fabrication of high-efficiency energy storage electrode in Li-ion and Li-S batteries.

Aimin Wu is an associate professor in School of Material Science and Engineering, Dalian University of Technology. He received his Ph.D. degree at Dalian University of Technology in 2002. He worked as a post doctor in University of Limoges, France in 2003. His current research is focused on the fabrication of various film materials applied in Lithium-ion batteries and fuel cells.

Kai Cheng was born in Shanxi, China in 1992. She is now pursuing Ph.D. degree under the supervision of Prof. Jijun Zhao at the Key Laboratory of Materials Modification by Laser, Ion and Electron Beams (Ministry of Education) in Dalian University of Technology. Her research interest mainly focuses on the computational materials science of nanostructures and lithium-ion battery electrode materials.

Xiaona Li is an associate professor of Dalian University of Technology and a fellow of Chinese Electron Microscope Society. Her research is concerned with the functional electronic films, metal silicide films and material microstructure analysis. Her present research is in two main areas: one is the composition design based on the cluster model, preparation and characterization of copper alloy films; the other is the semiconducting amorphous beta-$FeSi_2$-based bulk and film materials.

Xiaoxia Gao is a Senior Engineer in School of Materials Science and Engineering, Dalian University of Technology. She gained her Ph.D. in Materials Science and Engineering, from the University of Texas, at Austin in 2005. Her research mainly focuses on materials characterization and analysis with TEM techniques, especially on nanomaterials.

Jijun Zhao was born in Jiangsu, China, in 1973. He received his Ph.D. in condensed matter physics from Nanjing University in 1996 and became a professor in Dalian University of Technology in 2006. He is now director of the Key Laboratory of Materials Modification by Laser, Ion and Electron Beams (Ministry of Education). His major research field is computational materials science with special interest in clusters, nanostructures, and new energy materials. He has contributed over 300 refereed journal papers and his current H-index is 48.

Xinglong Dong is a professor of Dalian University of Technology. He obtained his Ph.D. at Institute of Metal Research, Chinese Academy of Sciences. His research work is focused on synthesis and characterization of core-shell nanoparticles, as well as the magnetic, electric, electromagnetic and electrochemical properties of nanocomposites.

Guozhong Cao is Boeing-Steiner professor of Materials Science and Engineering, professor of Chemical Engineering and adjunct professor of Mechanical Engineering at the University of Washington, Seattle, WA. He has published over 500 research papers and authored and edited 8 books and is one of the Thomson Reuters Highly Cited Researchers. His current research focuses on chemical processing of nanomaterials for solar cells, rechargeable batteries and supercapacitors, as well as actuators and sensors.